Materials Science and Engineering B 269 (2021) 115164

Contents lists available at ScienceDirect

Materials Science & Engineering B

journal homepage: www.elsevier.com/locate/mseb

Vanadium silicon-oxyfluoride nanowires for lithium storage systems: A perfect synergy for dynamic simple spot synthesis

Kiran Preethi Kirubakaran [a,b], Chenrayan Senthil [c], Subash Chandrabose Raghu [d], Marimuthu Priyadarshini [b], Shanmugasundaram Kamalakannan [b], Muthuramalingam Prakash [b], Chang Woo Lee [c], Kumaran Vediappan [b,*]

[a] Department of Physics and Nanotechnology, Faculty of Engineering and Technology, SRM Institute of Science and Technology, Kattankulathur 603203, Tamil Nadu, India

[b] Electrochemical Energy Storage and Conversion Laboratory (EESCL), Department of Chemistry, Faculty of Engineering and Technology, SRM Institute of Science and Technology, Kattankulathur 603203, Tamil Nadu, India

[c] Department of Chemical Engineering (Integrated Engineering) & Center for the SMART Energy Platform, College of Engineering, Kyung Hee University, 1732 Deogyeong-daero, Giheung, Yongin, Gyeonggi 17104, South Korea

[d] Vels Institute of Science, Technology and Advanced Studies, Pallavaram-600117, Tamil Nadu, India

ARTICLE INFO

Keywords:
Energy storage and conversion
Batteries
Electrode
Power density
$LiVSiO_4F$
Ultrafast synthesis

ABSTRACT

Polyanionic vanadium silicon oxyfluoride, $LiVSiO_4F$ (VSF) nanowire synthesize through a dynamic simple spot method exposes a multi-redox behavior with excellent reversibility and minimal capacity fade as electrodes in Li-ion systems. However, the cycling performance of the electrode is under debate due to its conductivity and polyanionic nature. To address this, an increase in the ratio of a conductive agent like 10%, 20%, and 30% is intermixed with cathodes, and as a result, the cathodes reveal an increasing electrochemical performance for VSF 30%. At a high current rate of $1Ag^{-1}$, VSF 20% and 30% express a specific capacity of 164 $mAhg^{-1}$ and 230 $mAhg^{-1}$ respectively, which is higher than the theoretical capacity. This is due to the anionic redox nature of O and F, apart from transition metal vanadium. VSF 30% exhibits a higher power density of $300Wkg^{-1}$ with an energy density of $623WhKg^{-1}$ that can be applicable in high-power devices.

1. Introduction

Lithium (Li)-ion rechargeable batteries sustain the modern society decade after decades, even though the entire science behind the mechanism is yet unidentified. Moreover, the records in terms of the development of batteries keep magnifying through the discoveries of novel and alternative electrode materials and electrolytes due to the increasing demand for high energy density and power density batteries with economic and environmental sustainability [1,2]. Supercapacitors are proved to possess higher power density, which seems like a critical factor for the start-up of heavy vehicles. On the other hand, batteries are capable of high energy density, promising the long-run for the electric vehicle. Indeed, it is challenging to fabricate an effective device that fulfils both the necessities and the researchers focus widely on this [3]. The electrode materials, majorly cathodes contribute a lot over the operation of the whole battery in terms of safety, cost, and energy density. Against this background, the development and innovation of efficient cathodes are a crucial one. In this regard, a cathode material is emphasized to obtain high energy density and power density [4,5]. Enormous works have been focussed on polyanionic compounds owing to their higher safety, structural and thermal stability, high voltage, etc [6–8]. Polyanionic compounds consisting of fluorine atoms, not only adds greater benefit to the overall stability of the material through the contribution of its highly electronegative nature but also helps with an increase in the electrochemical performance through voltage [9]. Tavorites are one of those structures with fluorine as one among the crystal composition. Most of the explored tavorites are fluorophosphate and fluorosulfates with a variety of transition metals in the crystal geometry [10,11]. The working potential along with the inductive effect between the polyanion and the ligand can be tuned in these tavorites by the utilization of various transition metals in the stoichiometry ($LiMXO_4Y$). Among which the vanadium based Tavorites have attracted greater attention than the other transition metals due to its excellent properties [12]. In addition, there are still a lot of works that has to be

* Corresponding author.
E-mail address: kumaranv@srmist.edu.in (K. Vediappan).

https://doi.org/10.1016/j.mseb.2021.115164
Received 23 November 2020; Received in revised form 3 March 2021; Accepted 29 March 2021
Available online 15 April 2021

focused to bring the most out of the unexplored Tavorites, since the most explored Tavorites are with the polyanionic presence of phosphates and sulfates. Herein, with the transition metal as vanadium and with the polyanion as silicates, a vanadium based silicon oxyfluorides are being focussed, and is believed that these structures would be able to increase an energy density as well as power density for Li-ion batteries due to its uniqueness [13,14]. LiVSiO4F has been computationally investigated by M.E. Arroyo [15] and experimental/electrochemical investigation through solid state method previously [16]. Currently, Vanadium silicon oxyfluorides(VSF) are prepared through a rapid and dynamic simple spot method using a microwave reactor to facilitate the economic and environmental sustainability [17]. The reaction duration was tailored by varying from 5 min to 30 min under a constant temperature of 150 °C through stable radiation.

2. Methodology

2.1. Experimental

2.1.1. Synthesis

$LiVSiO_4F$ (VSF) is prepared by the dynamic high-pressure microwave reactor (Anton Parr Multiwave pro). The precursors – LiOH, V_2O_4, SiO_2 and NH_4F are weighed based on stoichiometry and is dissolved in 80 mL of distilled water one over the other and kept for continuous stirring for a minimum of 30 min under a constant temperature of 60 °C. The obtained solution is then transferred to a Teflon test tube and is set into the microwave reactor. The reaction was processed under variable reaction duration with an interval of 5 min at a constant temperature of 150 °C. The product obtained with a reaction time of 15 min has been finalized and is named VSF (**Fig. S1**) [18].

2.1.2. Characterization techniques

Powder X-ray diffraction (PXRD) analyses were recorded on (PXRD, PANalytical India, Spectris Technologies) with Cu Ka radiation (λ ¼1.5406 Å). FTIR spectra were obtained in the range from 400 to 4000 cm^{-1} by a Fourier transforms infrared (FTIR) spectrophotometer (PerkinElmer Spectrum One, Perkin- Elmer Co., USA). Cyclic Voltammetry (CV), charge-discharge and Electrochemical Impedance Spectroscopy (EIS) studies of half-cells were performed on a Biologic electrochemical workstation (BioLogic–SAS, VSP-300), Neware battery testing instrument (Neware, BTS4000, China) and (Origa flex OGF500 & OGF10A), Origalys Electrochem. France.

2.1.3. Cathode fabrication

The positive electrode material was fabricated by the grinding of active material (VSF), Carbon black (conducting agent), PVDF binder in 8:1:1 ratio until a homogeneous mixture is obtained. It then proceeds for the preparation of viscous slurry using NMP as a solvent. The slurry is then coated onto the aluminium foil (current collector) and vacuum dried overnight at 80 °C. The dried electrode was flattened using a Dual-roller Electric Calendaring Machine, TMAX, China, and was punched out with a diameter of 15 mm. The punched electrodes were then dried again at 80 °C for 6 h to remove the excess impurities. The material with 10%, 20% and 30% carbon black is named VSF 10%, VSF 20% and VSF 30%. The conductive agent was not taken beyond 30%, since the carbon black may dominate the whole electrochemistry than the VSF cathode materials.

2.1.4. Coin-cell assembly:

The dried electrodes were used as a cathode during the coin cell fabrication inside the argon-filled glovebox (Nichwell α-1800(α-1800P-P-400R) (4 Ports), USA). The Li metal foil, GF (glass fiber), and 1 M $LiPF_6$ in EC: DMC (1:1) served as the counter electrode, separator and electrolyte respectively, during the half-cell fabrication and these were assembled and crimped to obtain a standard CR2032-coin cell [16].

2.2. Computational

The DFT calculations on the periodic $LiVSiO_4F$ crystal structure were computed by projector augmented wave (PAW) pseudo potentials which are implemented on the VASP [19,20] program. This PAW [21,22] method was used to represent the core and valence electrons of the cathode material. The exchange correlation functional are expressed by Perdew – Burke – Ernzerhof [23] (PBEsol) with generalized-gradient approximations (GGA) and the hybrid functional of Heyd-Scuseria-Ernzerhof (HSE06) [24,25] which are used to opens the band gap of the tavorite material. The energy 500 eV cutoff was fixed for all electronic structure calculations and structural relaxations of $LiVSiO_4F$ material were done by the conjugate algorithm until forces on all atoms were below 0.01 eV/Å. The Brillouin zone sampling of the tavorite material was carried out by 3 × 3 × 2 Γ-centered through Monkhorst-Pack [26]. The Hubbard-U method was adopted to interpret the strong correlation among the d electrons of the vanadium atoms. The effective U values of vanadium (V) and lithium (Li) atoms are 3.0 and 4.0, respectively, which are obtained from earlier reports [27–29].

3. Results and discussion

3.1. Physical

Fig. 1**a** depicts the XRD pattern of VSF obtained with a reaction duration of 15 min, which was optimized for further investigation due to the reason of minimal secondary products. The diffraction peaks observed in the XRD pattern correlate well with standard JCPDS cards for compounds $LiVO_3$, Li_2SiO_3, LiF and SiO_2, confirming that the final product has been formed with the presence of every desired element [16]. To further understand the material's stability with respect to temperature, the TGA-DSC plot (Fig. 1**b**) is preferred. From the TGA curves, a weight loss of about 3.29% is observed at 200 °C due to the presence of moisture in the sample. Later, at the end of 500 °C, a total of 9.4% weight loss is resulted due to the removal of secondary products. Besides, most of the peaks in the DSC plot states that the reaction is processed in an endothermic nature with a positive enthalpy [30]. On the whole, VSF manages to possess good thermal stability with a weight loss of only 11.94% at the end of 900 °C. This particular stability drives for the VSF to have a prominent electrochemical result even at sensitive mode operations. XPS analysis was performed to further analyse the chemical composition of the sample and majorly vanadium, as it is the element accountable for the redox reactions. From the V2p spectrum, it is observed that the peak exhibited at 524.2 and 525.8 eV corresponds to $V2p^{1/2}$ whereas the peak at 518 eV is of $V2p^{3/2}$(Fig. 1**c**). Thus, it is evident that the material possessed V^{4+}/V^{5+} oxidation states. Also, due to the presence of oxygen in the poly-anionic compound, these peaks are found to be influenced by V-O bonds. Considering the Si2p spectrum, two peaks were observed at 100.6 eV and 104.8 eV, which are owed to the bonding nature of O with Si to form SiO_2. The peak visualised at 531 and 533.3 eV in the O1s spectrum pertains to that of metal oxides, while F1s spectrum expose peak at 686 eV which corresponds to the existence of oxyfluorides (Fig. 1**d-f**) and the XPS analysis for the other elements are provided in **Fig. S2** [31,32].

It is well-known that the morphology being one of the foremost contributor towards the intense electrochemical reactions [33], VSF is found to be of wire-like structures with the nanoscale dimension through microscopic studies such as FE-TEM and FE-SEM. Apart from the nanowire morphology, a few solid blocks are also visible in the FE-SEM images of VSF. It is a known fact that the nanomaterials easily tend to agglomerate or aggregate. Hence, this dual morphology can be attributed to the aggregation of nanowires to result in a bulky morphology. Further, in Fig. 2**c, a** single nanowire is observed with a diameter of about 75 nm. **Fig. S3** displays the histogram stating the average particle size to be 6.954 nm. The elemental mapping images are showcased in Fig. 3 for all the elements, and their corresponding atomic percentage

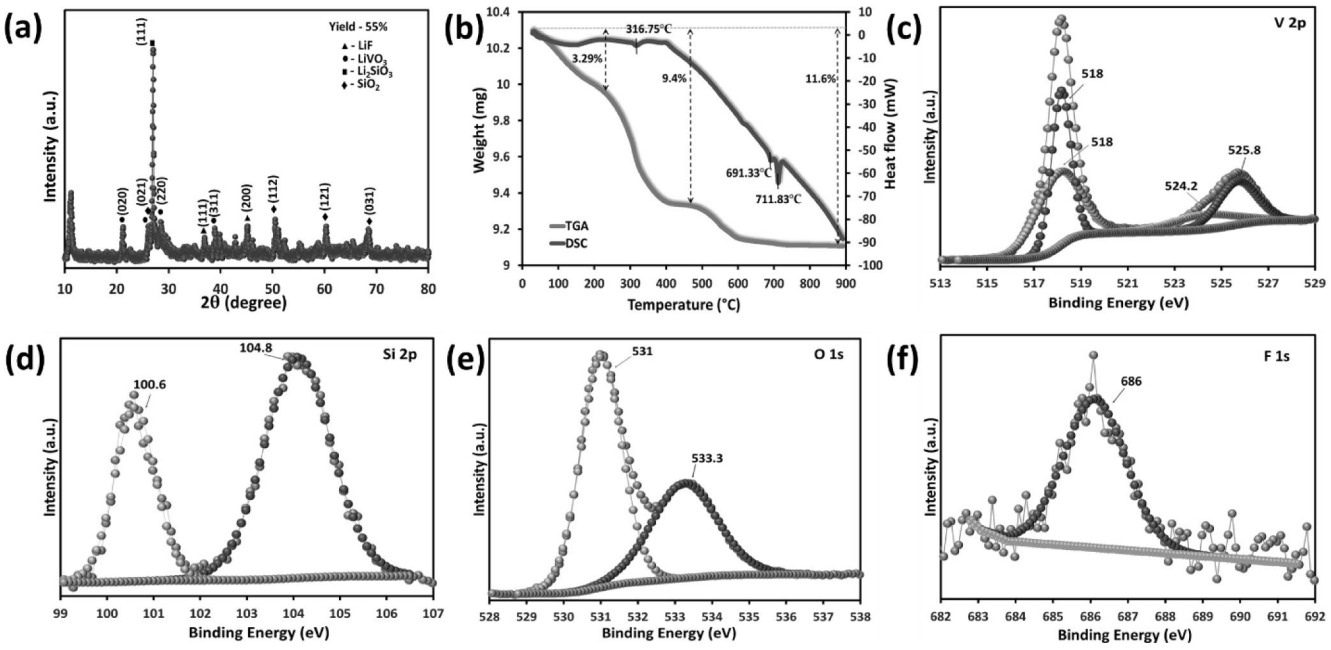

Fig. 1. (a) XRD pattern (b) TGA-DSC profile and XPS spectrum of (c) V 2p, (d) Si 2p, (e) O 1 s, (f) F1s, for VSF (Vanadium silicon oxyfluoride).

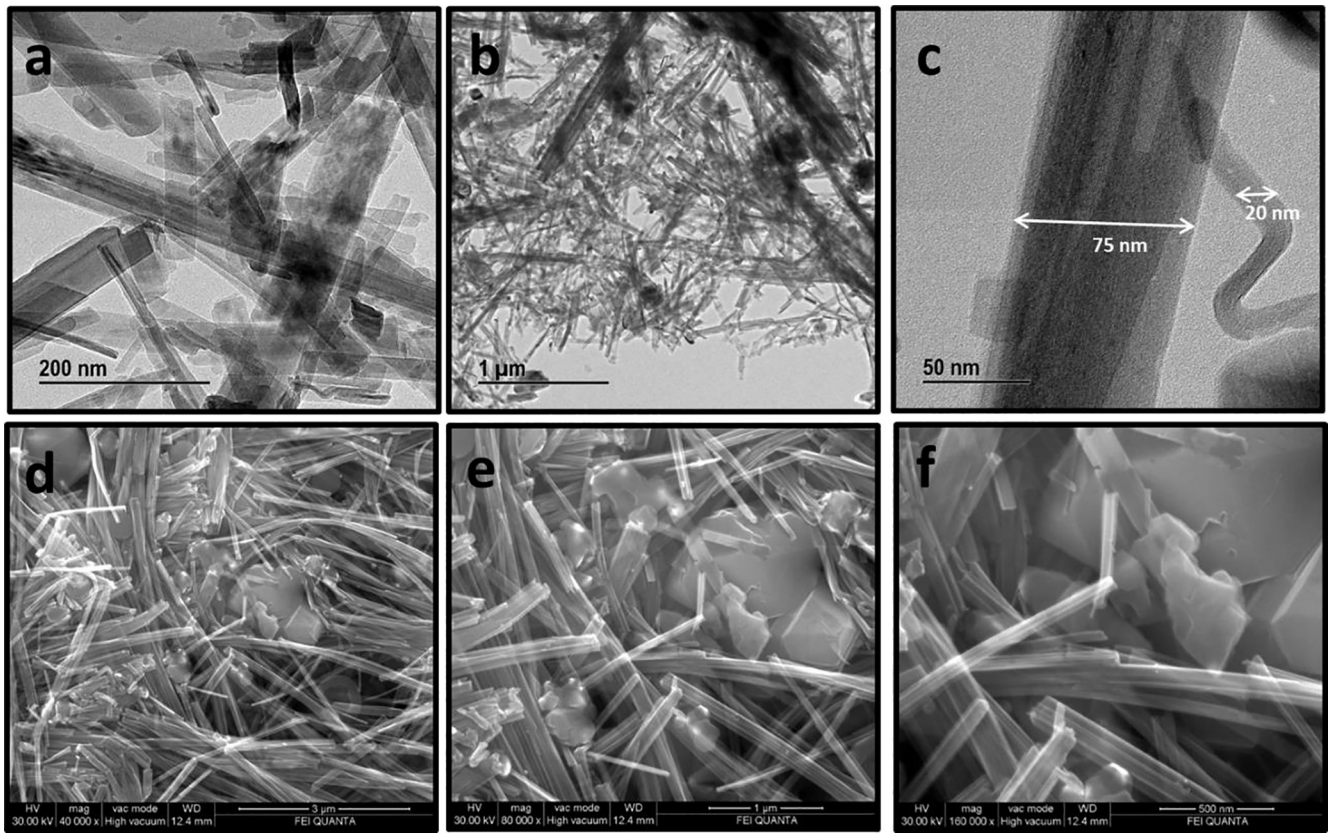

Fig. 2. FETEM images at (a) 200 nm, (b) 1 μm, (c) 50 nm and FESEM images at (d) 3 μm, (e) 1 μm and (f) 500 nm of VSF.

obtained from EDXA.

3.2. Computational

To have a better understanding of the crystal structure of the material, the structure is computationally obtained and the optimized geometries are shown in Fig. 4**a**. The partial electron density of states (PDOS) of VSF (Fig. 4**b**) and the PDOS plots of individual atomic species (Fig. S4) are calculated. It is found that the overlap contribution of V and O atoms to PDOS is close to the Fermi region which is significantly higher than the other atoms in VSF. For example, other atoms such as Li, F, and Si contribute very little in PDOS near the Fermi region. Among

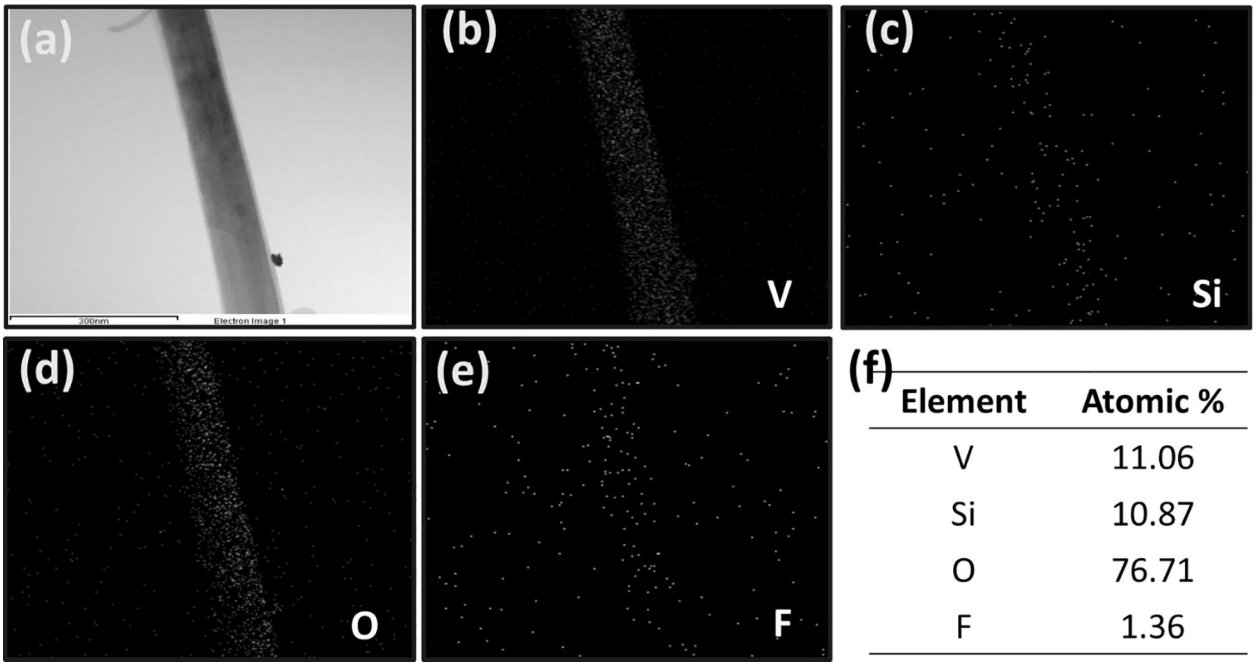

Element	Atomic %
V	11.06
Si	10.87
O	76.71
F	1.36

Fig. 3. (a-e) Elemental mapping FESEM image of a single nanowire displaying the presence of elements V, Si, O, and F; (f) atomic percentage of elements obtained from EDXA.

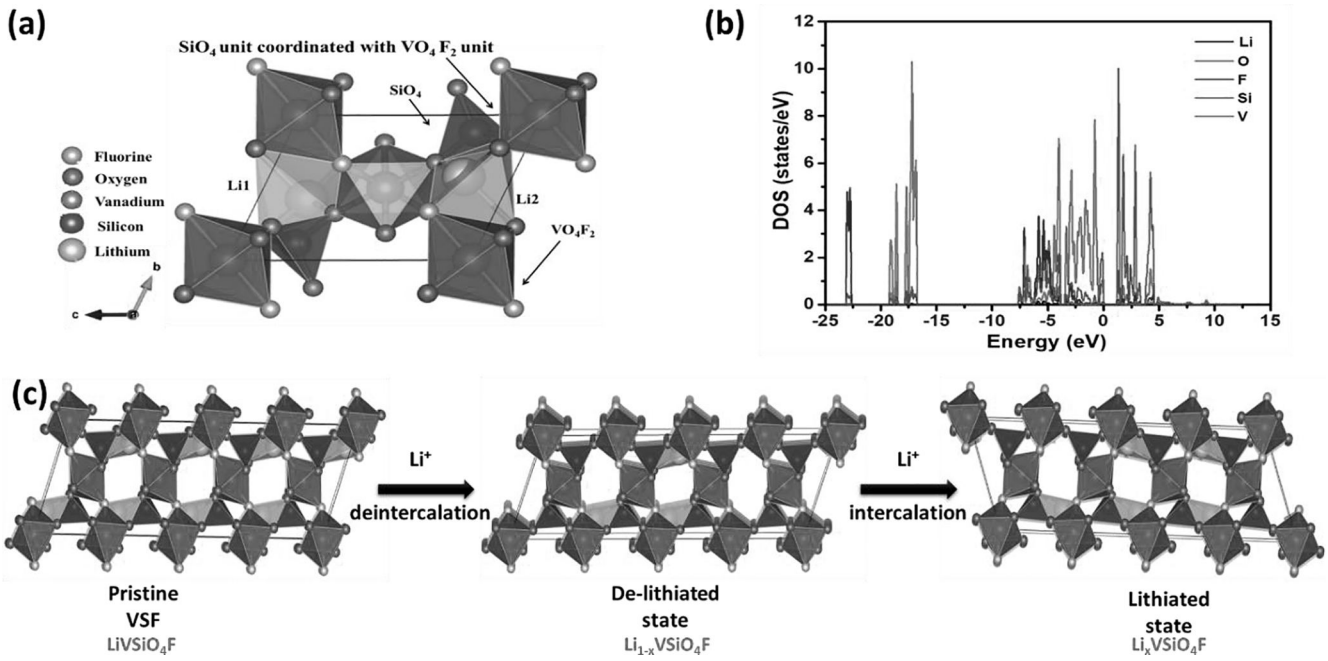

Fig. 4. (a) Optimized geometries of crystal structure were computed, the individual atoms are represented by different colors; (b) Total partial electron density of states (PDOS) of VSF, the different colors of peaks represent the individual elements presented in the crystal unit; (c) Schematic of Li^+ intercalation/de-intercalation in VSF.

these, F atom displays a slightly higher contribution particularly in positive energy levels near the Fermi region. This may be due to the higher number of electrons (or lone pair electrons) present in fluorine when it is compared to the lithium and silicon. Further, the higher contribution arising from V, O, and F atoms near to the Fermi region is anticipated to play a critical role in the anionic redox behavior of the material [34,35]. The electronic properties of VSF are analyzed by the band structure which is calculated by high symmetry K-points across the first Brillouin zone. The calculated band structure of $LiVSiO_4F$ is presented in Fig. S4. It shows that the Fermi level is very close to the zero point, and VSF behaves as a semiconductor with an energy gap of 1.25 eV. This computed value is in good accordance with the previous theoretical reports on pristine $LiVPO_4F$, which is 1.75 eV. In the band structure the bottom of the conduction band and the top of the valence band recline on Γ and X points of the first Brillouin zone, respectively. Thus, VSF is a semiconductor with an indirect band gap. The experimental band-gap of VSF is identified using the Tauc plot through UV-Vis spectroscopic technique (Fig. S4g). The band gap was determined to be

4 eV for VSF 20%, which confirms its insulating nature. This nature has benefitted the electrochemical behaviour by the decreased reactivity of the cathode material with electrolyte and facilitating higher diffusion with negligible side reactions inside the battery system.

3.3. Electrochemical

Poly-anions, being a class of emerging structures, offer a great range of benefits for the electrochemistry of the material. Hence, VSF is expected to perform well on grounds of its poly-anionic behavior. In general, the electrodes for a battery constitute of a conductive carbon and binder in minor amount along with majority of active material, where the inclusion of conductive carbon is extensively proved to improve the conductivity of the electrode. In our case, poly-anionic cathode materials are known to suffer from conductivity issues, thus the conductive agent (carbon) was preferred in order to further increase the conductivity of the VSF cathodes for the better performance of the battery system. Hence, VSF has been fabricated with different ratios of conductive agent-carbon black (CB) and are named as VSF 10%, VSF 20% and VSF 30% (with 10, 20 and 30% of CB in it). By default, VSF possessed 10% of carbon black. To examine VSF on the capability to act as a positive electrode for Li-ion batteries, a series of electrochemical techniques were performed at room temperature. Cyclic voltammogram (CV) results unveil the excellent redox property with multiple peaks for reduction and oxidation. Fig. 5**a** displays the CV of VSF 10% at a scan rate of 0.1 mVs^{-1} in 2.0–4.5 V potential range. As deduced from the voltammogram curves, four distinct peaks were observed at 2.6 V, 2.9 V, 3.2 V and 3.6 V for oxidation and 2.3 V, 2.6 V, 3.1 V and 3.5 V for reduction processes. At the end of 6 cycles, all the peaks are well retained proving the reversibility of the material, except for the fact that the reduction peak at 3.1 V is slightly suppressed, which might be due to the influence of side products that get decomposed/passivated later. It is worth mentioning that the as-prepared polyanionic materials are capable of undergoing multiple Li-ion intercalation/de-intercalation, thereby it can enhance the electrochemical kinetic performance of a battery. Further, the voltammogram revealed that the VSF is highly electro-active with the majority of the couple due to V^{4+}/V^{5+} redox behaviour. These results also correlate well with the V2p XPS spectra of the material [36]. The CV profile of VSF 20% and VSF 30% is displayed in Fig. S4. Fig. 5**b** depicts the comparative galvanostatic charge/discharge profile of VSF at a rate of 1C with a cut-off voltage of 2.0–4.5 V for the second cycle. From the profile, it is clear that it coerces well with the CV graph showcasing the redox peaks with plateaus. To promote this, dQ/dV graph is plotted and can be seen in Fig. 5**c**. A specific discharge capacity of 92, 95 and 103$mAhg^{-1}$ is obtained for VSF 10%, 20% and 30% respectively, while the theoretical specific capacity of the materials stood at 158.6$mAhg^{-1}$. Furthermore, an increase in the percentage of a conductive agent is found to increase the specific capacity of the material. Additionally, it also aided in the achievement of higher energy density and power density for the VSF cathodes, by mitigating the side reactions and increasing reversibility [16,37–39]. This states that conductivity acts as one of the crucial roles in the electrochemical performance of VSF. In comparison to the other cathode materials that are already available, VSF possesses the capability to achieve excellent reversibility of Li-ions during insertion/extraction kinetics, which results in a very negligible capacity fading that is mainly attributed to the structurally stable geometry of VSF. To support this statement, the stability of VSF is calculated by bader charge transfer analysis computationally. The corresponding values are given in Table. S1. The calculated net charge of Li1 and Li2 atoms in the VSF structure is + 1.00 e, which is exactly close to the reported theoretical value. From these results, it is clearly evident that the formation of the ionic Li-O bond is due to the coulombic effect [40]. The computed net charges of V, O and F ions in VO_4F_2 of $LiVSiO_4F$ structure clearly confirms the existence of the octahedral units in the crystal structure. This reaffirms that the stability of VSF is caused by VO_4F_2 owing to the strong molecular covalent interaction. The comparative cycle life plot is shown in Fig. 5**d** where a similar capacity of 56–60% is retained for all the cathodes while their coulombic efficiency is approximately ~ 99%. As observed, all the compositions of VSF electrodes exhibit decay in the specific capacity. In terms of battery chemistries, the use of carbon as conductive agent promotes not only the conductivity but also the volume changes, however in the case of VSF, the degradation in the specific capacity is rather a phenomenon promoted by the activity of cationic and anionic species, namely the V, O and F, respectively. This aspect could be understood better in terms of correlating the electrochemical characteristics with the theoretical studies. Considering the theoretical calculations, the higher contributions of elements V, O and F towards the Fermi level is

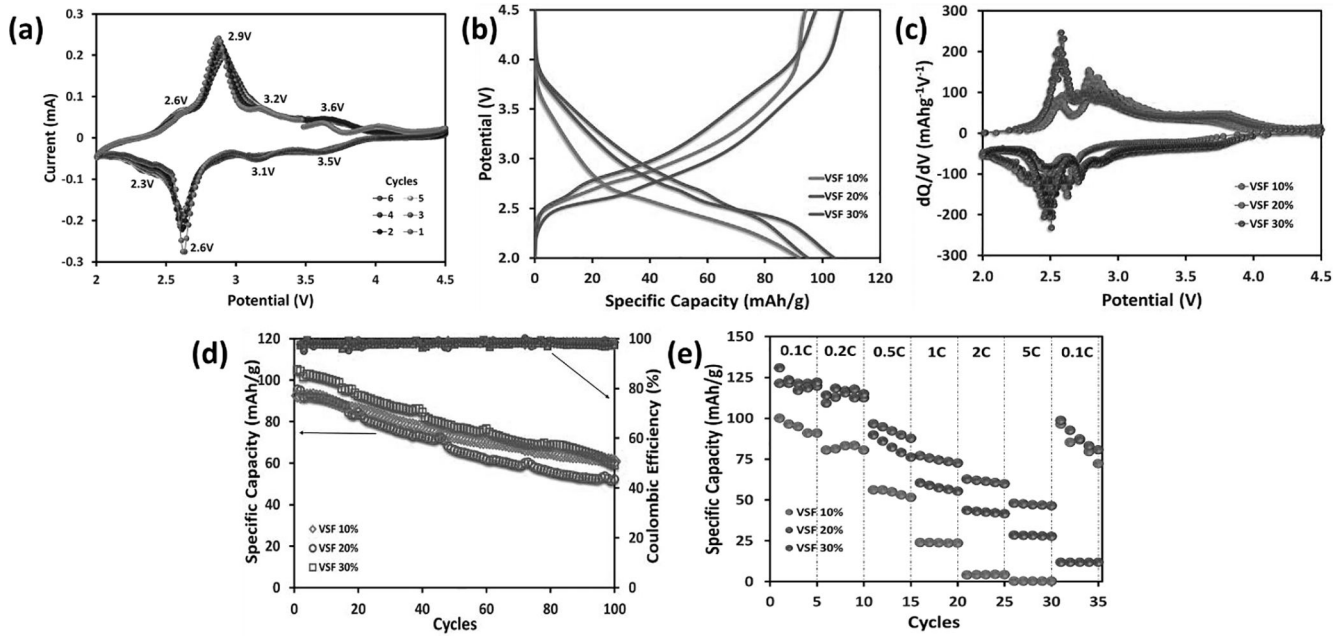

Fig. 5. (a) Cyclic voltammogram of VSF 10%, (b) comparative charge-discharge profile at 1C rate, (c) dQ/dV plot (d) long-term cycling graph with corresponding coulombic efficiencies, (e) comparative rate capability profile of cathodes.

anticipated to have a greater role towards the anionic redox behaviour (**Fig. S5,** S4), thus the VSF could undergo both cationic and anionic redox process within the battery system. These theoretical results are validated experimentally through the electrochemical studies involving cyclic voltammetry, charge/discharge and differential analysis (Fig. 5). Considering the voltammetry and differential studies, there appears redox contribution at higher potential around 3.5 V which is also owed to the participation of anionic species in the electrochemical reaction. Apparently, these anionic redox behaviours along with the regular cationic redox process expose the high specific capacity to the VSF electrodes [41,42]. However, with an increase in the cycle numbers, the contribution from anionic species F becomes more vulnerable with the electrolytic system to form more inactive species leading to capacity degradation to the VSF electrodes in spite of the presence of carbon [40]. Fig. 5**e** displays the comparative rate capability profile of all cathodes. The profile shows that VSF 10% and 20% is retainins the specific capacity back to 0.1C, after its subjection to higher current densities while VSF 30% did not retain. This is attributed to the huge volume expansion of the cathode material upon addition of higher percentage of carbon into it (exceeding the saturation point). It relates well with the band gap of the cathodes. And this gradually leads towards structural distortion making the material difficult to withstand higher current densities. The volume expansion was calculated previously for VSF as 21.9%. An addition of carbon into the VSF electrodes would result in a higher percentage of volume expansion, thus making it obvious that the structural and anti-site defects take place for VSF 30%. Consequently, VSF 20% ascertains as a rate-capable cathode material than its analogues (VSF 10% and VSF 30%) by a better specific capacity retention [16]. It also confirms that a 20% of conductive agent addition does not bring any commotion and serves as a saturation point, beyond which the volumetric expansion happens causing a variety of electrochemical issues.

Fig. 6**a-b** displays the cycling graph of VSF 20% and VSF 30% at a higher current density of $1Ag^{-1}$. It is observed that the specific capacity is higher for few initial cycles, after which the specific capacity falls back. This deviation can be reasoned with many side reactions that occur due to the stable intermediates during the discharge [44]. **Fig. S6a** reveals the comparative long-term cycling plot obtained by cycling at high current rate of $1Ag^{-1}$ for 200 cycles. It is observed that the specific discharge capacities are 84, 164 and 230mAhg^{-1} for VSF 10%, 20% and 30% for the 2nd cycle, and 78, 104 and 68mAhg^{-1} for the 200th cycle respectively.Unlike most cathodes, the specific capacity does not fall to the lowest value even under higher current density and prolonged usage [14,45]. Even though VSF possesses less theoretical capacity, it proves its strength by its cycling performance at a high current density of $1Ag^{-1}$. Upon subjecting the Li-ion cells to higher current loads, the specific capacity increased when it is compared with the specific capacity obtained at lower current loads, which might be associated to the electrochemical participation of both VSF and carbon to deliver improved performances. It is worth to mention that the higher charge/discharge capability of the electrode is anticipated through the involvement of carbon along with the VSF active material which cumulatively aids in storing the charges at higher current loads through the non-faradaic process that occur at carbon (non-redox process) and faradaic process at VSF (redox process). Thus, the electrodes exhibited an improved charge storage behaviour at higher current loads than the

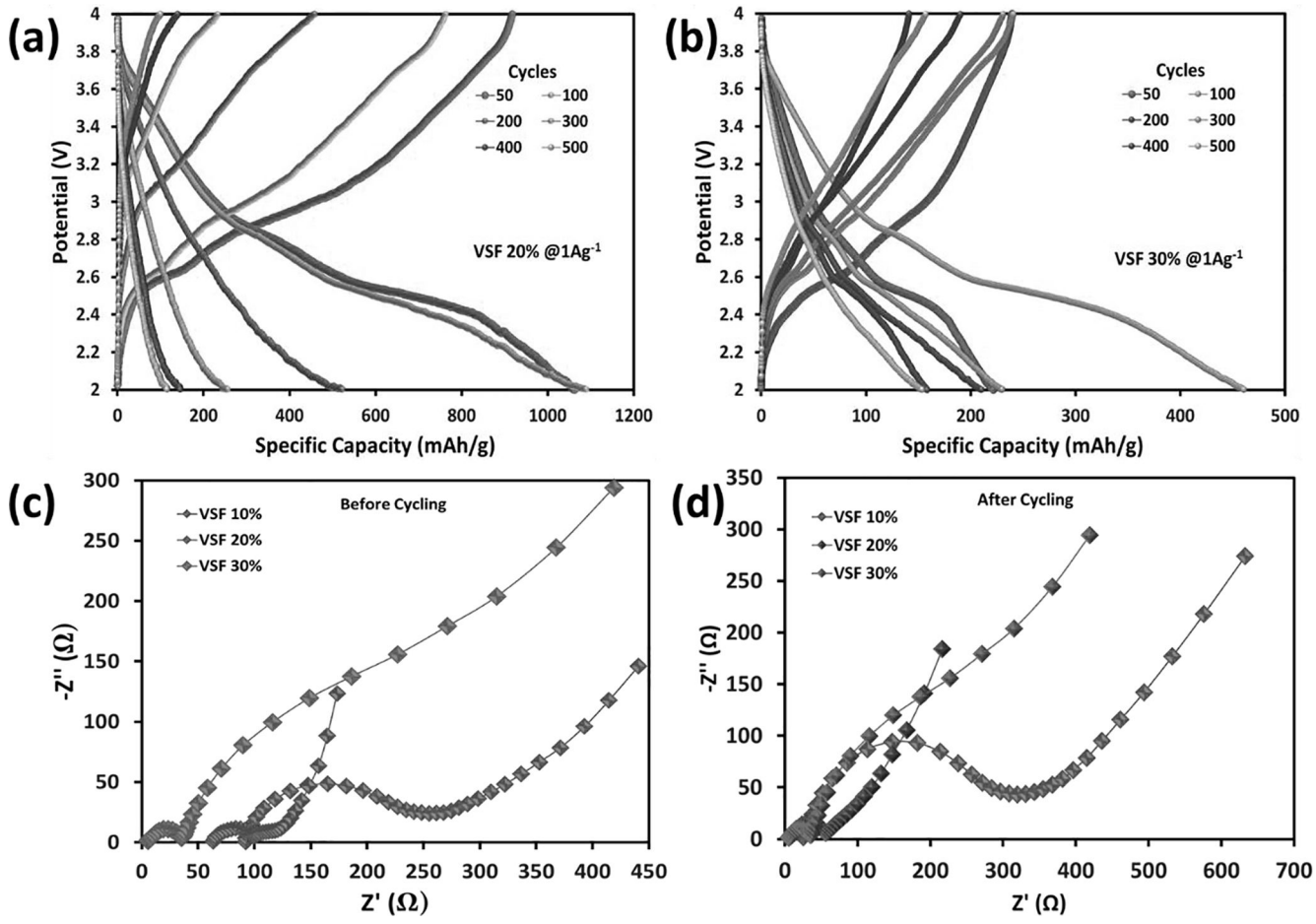

Fig. 6. Charge-discharge profile at $1Ag^{-1}$ of (a) VSF 20% and (b) VSF 30%; EIS graph (c) before cycling and (d) after 100 cycles for VSF 10%, 20% and 30% respectively [43]

lower current [46]. Moreover, the occurrence of these fluctuations especially at high current rate is because that the cathode material is also highly influenced by the drastic current imposed on it. This further leads in disturbance to the electrodes causing variation on the current generated at the electrode surfaces [47]. Additionally, the lower current loads does not cause severe diffusion and migration of ions and electrons, thus they move favourably, whereas the higher current loads agitates the whole electrode system with facile kinetics of ions and electrons which makes the carbon to involve in non-faradaic charge storage which leads to higher specific capacity. From these values, it is notable that the VSF 20% and 30% exhibits a capacity that is even higher than their theoretical capacity, this particular deviation occurs only at higher current density. The possible solutions might be: (a) the redox behaviour of anionic elements O and F apart from cationic V. As deduced through the computational studies, the results of the band structure calculations termed that V, O and F play a major role in redox reactions. Hence, it is suspected that when too much of current density is applied, restructuring takes place, so that O and F participate in an anionic redox reaction as well. Similarly, there might be the possibility of other elements that are present in the electrolyte to take part in short-term reactions [48,49], (b), as per Deng et al, a structural reformation intervenes during Li^+ insertion into VO_4F_2, which possibly minimizes the polarization leading to a higher voltage [37]. Thus, this may serve as one of the essential idea of exploring VSF to the finest electrode. The highest power density of 300WKg^{-1} is exhibited by VSF 30%, while its energy density being 623WhKg^{-1}, which is higher when compared to LCO ($LiCoO_2$) and LFP ($LiFePO_4$) [50]. Such an interesting property of VSF to be triggered and tuned by the current density to produce higher power and energy density is displayed with the help of Ragone plot for VSF 10%, 20% and 30% as given in **Fig. S6**. The EIS spectra for the cathodes obtained before and after 100 cycles are displayed in Fig. 6**c-d**. The EIS plot consisted of a depressed semicircle starting at the high frequency followed by a low frequency slope. The initial gap left in the EIS plot on the x-axis is a sign of solution resistance (R_s), which is majorly due to the electrolyte and intrinsic resistance inside the cell. As supposedly known, the internal resistance is in the order of VSF 10%> VSF 20%>VSF 30%. This correlates well with the electrochemical results as discussed above. It also states that the inclusion of conductive agent to VSF has a positive influence on the battery by the decreased R_s. The diameter of the semicircle indicates the effect of charge transfer resistance (R_{ct}) due to the continuous flow of Li-ions inside the battery system. Warburg resistance (W) which occur during the low frequency is depicted by the slope. In ideal cases, the slope is always inclined at 45°, where a perfect diffusion takes place. Fig. S6c depicts the derivation of R_s and R_{ct} from the EIS plot along with its equivalent circuit. As seen in the EIS plot above, the slope is not ideal, indicating the possibilities for bizarre Li-ion diffusion. The EIS spectra performed after cycling studies show a very large resistance on the whole for all the cathodes, which is majorly due to the solid electrolyte interface and dead Li deposition on the interface [43,51].

Fig. 7 visualizes the relation between the performances of the VSF nanowires with the increasing ratio of conductive agent. It is evident that the increase in conductive agent to VSF, influences the morphology. This addition of carbon to VSF nanowires can neglect the interfacial bonding strength, thereby more space for Li insertion/extraction. It is expected that the carbon is in close proximity with nanowires through weak intermolecular forces. As the carbon content increases, the diameter of nanowires increases while their length decreases. This eventually leads to better conductivity for the electrodes while their bandgap moves towards a lower value. Also, a lot of factors such as mechanical stability, mobility, carrier concentration and diffusion can also be enhanced [52,53]. This might be the justification for an increasing order of power density exhibited by the VSF cathodes as seen in Fig. S6.

3.4. Kinetics

The comparative time vs. potential plot (Fig. 8**a**) disclosed the voltage drop that existed. Also, it shows that the voltage drop decreases

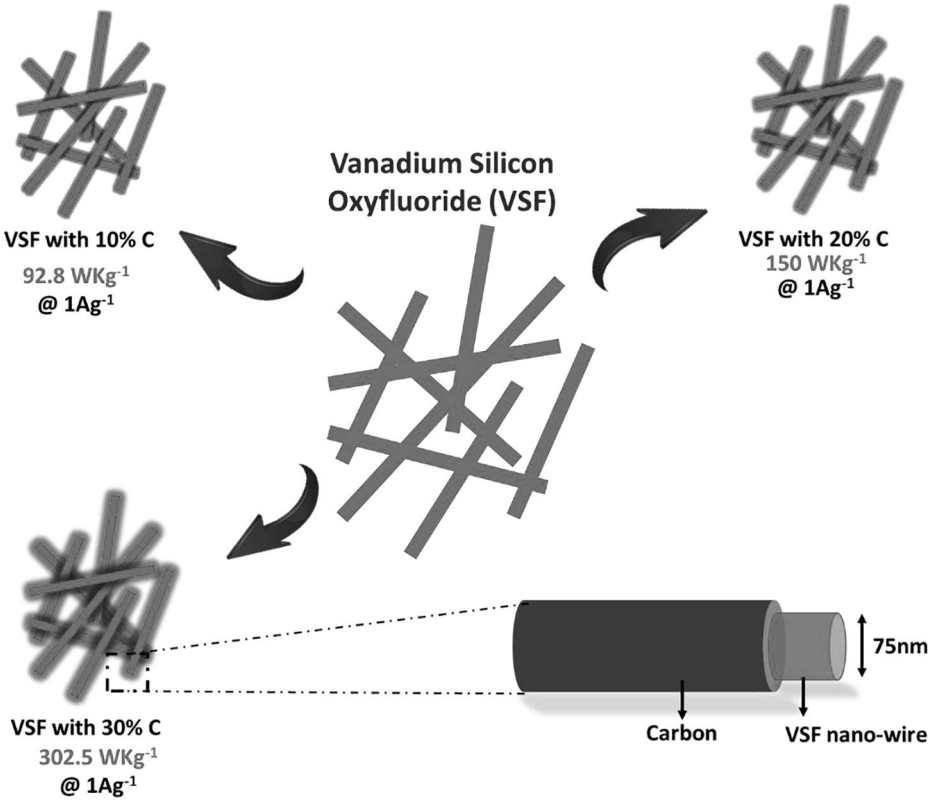

Fig. 7. Visualization of VSF nanowires with respect to the addition of conductive agent (Carbon) and their influence on power density.

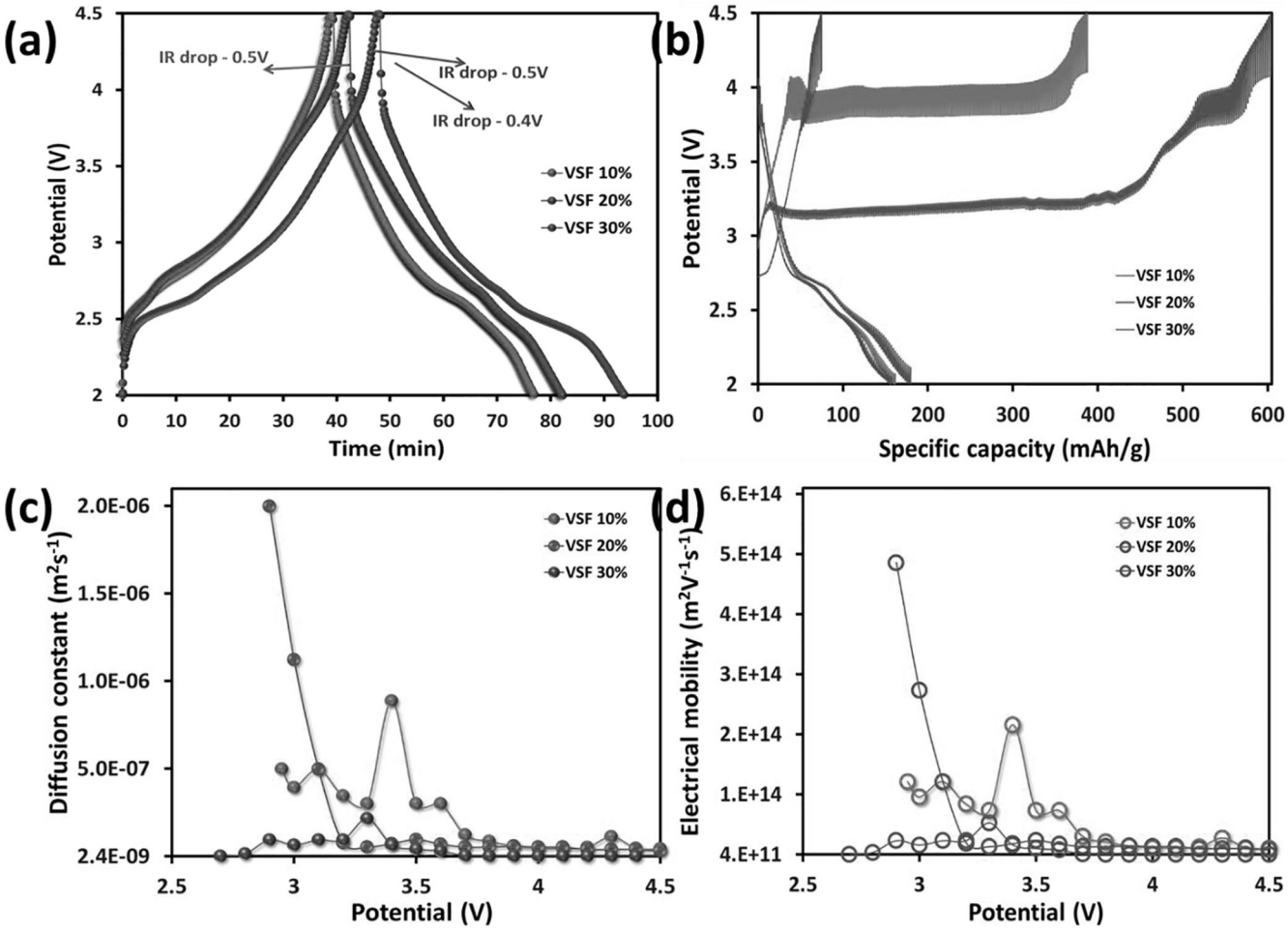

Fig. 8. (a) Comparative time vs potential plot, (b) GITT graph, (c) diffusion constant over potential and (d) electrical mobility for VSF 10%, 20% and 30% respectively.

with increasing conductivity. Additionally, to study the kinetics of the electrodes, GITT was performed in the voltage range 2.0 to 4.5 V at 0.1C rate with a relaxation period of about 10 min. The GITT profile is shown in Fig. 8**b** displays a lengthy horizontal region during the charge at 3.2 V and 4 V as a consequence of polarization and heavy internal resistance experienced by the cathode. It can also be assigned to the chemical crossover from anode to cathode and vice versa, thereby inhibiting the mobility of charge carriers. The GITT profile of VSF 30% can be viewed in **Fig. S7** for a detailed vision. In terms of specific capacity, the results displayed (Fig. 8b) are slightly deviating as the GITT profile of VSF 10% and 20% yields a higher capacity than 30%. Also, this does not affect the optimized 30%, since it is free from voltage restrictions and polarization to yield a stable performance, while 10% and 20% suffer from the same. From the GITT studies, it is known that the VSF as cathode material possesses certain drawbacks at lower current density (which is reaffirmed with cycling behaviour at lower current density-**Fig. S8**). Fig. 8**c, d**, unveils the diffusion coefficient and electrical mobility over potential respectively [54]. It is evident that, both the diffusion and mobility is higher at redox potentials while they are stable at other voltage conditions. This is majorly because of the release of ions caused by reversible reactions leading to higher mobility [55]. Fig. 9 demonstrates the development of Vanadium silicon-oxyfluoride nanowires for Lithium-ion batteries as a cathode active material through a schematic representation.

4. Conclusions

In summary, this work provoked the polyanionic material in order to meet the commercialization demands during the material manufacturing and various possibilities to explore cathodes with higher power density. VSF, synthesized by a dynamic simple spot synthesis route, exposed the multi-redox behaviour with both anionic and cationic participation in electrochemistry. Further, the material showed high rate capability, thermal stability, reversibility, 99% coulombic efficiency and high power density. In addition, the computational and kinetic parameters have also been investigated. On the whole, VSF cathodes can be tuned by the application of current density to provide higher power densities. Consequently, tunable VSF cathodes with multiple redox behavior may open new approaches towards the high rate lithium-ion storage applications.

CRediT authorship contribution statement

Kiran Preethi Kirubakaran: Conceptualization, Methodology, Investigation, Writing - original draft. **Chenrayan Senthil:** Visualization, Writing - review & editing. **Subash Chandrabose Raghu:** Visualization, Writing - review & editing. **Marimuthu Priyadarshini:** Visualization, Writing - review & editing. **Shanmugasundaram Kamalakannan:** Methodology, Investigation, Writing - original draft. **Muthuramalingam Prakash:** Supervision, Writing - review & editing. **Chang Woo Lee:** Visualization, Writing - review & editing. **Kumaran Vediappan:** Conceptualization, Project administration, Supervision,

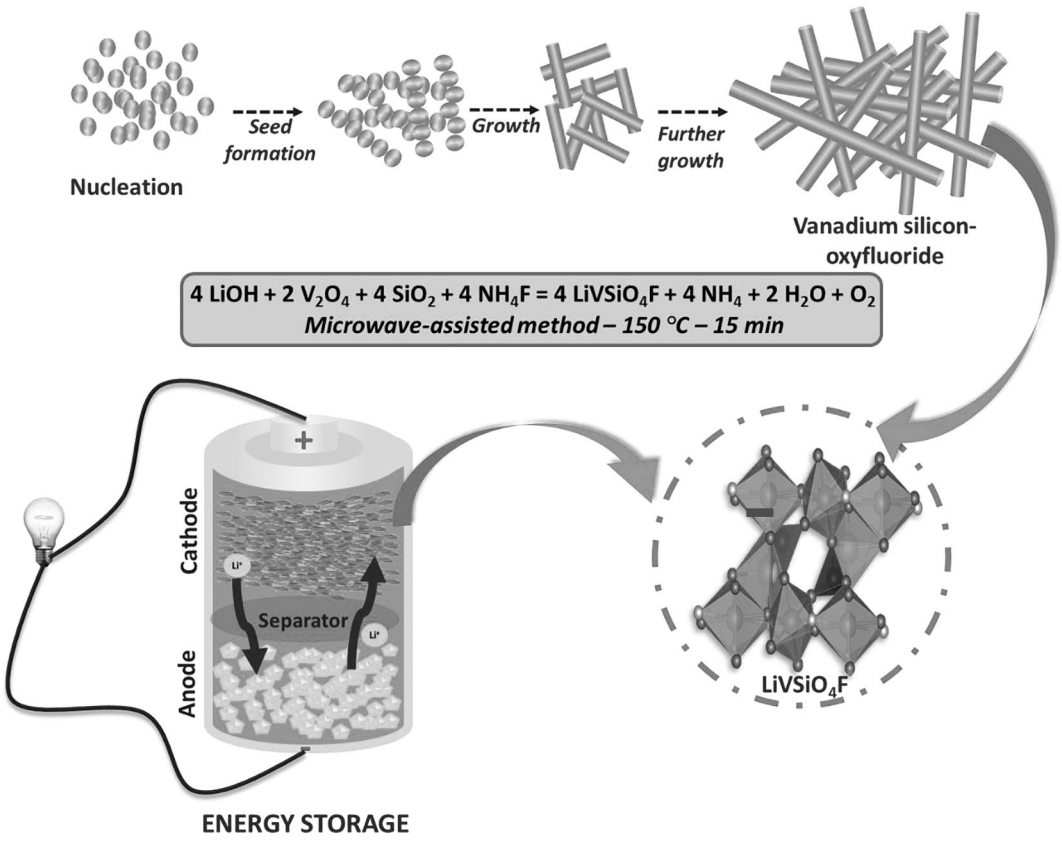

Fig. 9. Schematic representation of Vanadium silicon-oxyfluoride nanowires for Lithium storage systems.

Writing - review & editing.

Declaration of Competing Interest

The authors declare that they have no known competing financial interests or personal relationships that could have appeared to influence the work reported in this paper.

Acknowledgments

This research was supported by the Department of Science and Technology-Science and Engineering Research Board (DST-SERB), New Delhi, India (File No: ECR/2017/000095/ES). The authors acknowledge the SRM Central Instrumentation Facility (SCIF) from SRM IST, Chennai and thanks KHU Central Instrumentation facility at South Korea.

Appendix A. Supplementary data

Supplementary data to this article can be found online at https://doi.org/10.1016/j.mseb.2021.115164.

References

[1] W. Feixiang, M. Joachim, Y. Yu, Guidelines and trends for next-generation rechargeable lithium and lithium-ion batteries, Chem. Soc. Rev. (2020), https://doi.org/10.1039/c7cs00863e.
[2] J. Jiang, G. Nie, P. Nie, Z. Li, Z. Pan, Z. Kou, H. Dou, X. Zhang, J. Wang, Nanohollow carbon for rechargeable batteries: Ongoing progresses and challenges, Nano-Micro Lett. 12 (2020), https://doi.org/10.1007/s40820-020-00521-2.
[3] C. Choi, D.S. Ashby, D.M. Butts, R.H. DeBlock, Q. Wei, J. Lau, B. Dunn, Achieving high energy density and high power density with pseudocapacitive materials, Nat. Rev. Mater. 5 (1) (2020) 5–19, https://doi.org/10.1038/s41578-019-0142-z.
[4] M. Walter, M.V. Kovalenko, K.V. Kravchyk, Challenges and benefits of post-lithium-ion batteries, New. J. Chem. 44 (5) (2020) 1677–1683, https://doi.org/10.1039/C9NJ05682C.
[5] Y. Wang, X. Di, X. Gao, X. Wu, Design of MOF-derived hierarchical Co@C@RGO composite with controllable heterogeneous interfaces as a high-efficiency microwave absorbent, Nanotechnology 31 (2020), 395710.
[6] W.-S.-Y. Wontae Lee, S. Muhammad, C. Sergey, H. Lee, Jaesang Yoon, Y.M. Kang, Advances in the cathode materials for making a breakthrough in the Li rechargeable batteries, Angew. Chemie - Int. Ed. (2019), https://doi.org/10.1002/anie.201902359.
[7] Y. Wang, X. Di, X. Wu, X. Li, MOF-derived nanoporous carbon/Co/Co3O4/CNTs/RGO composite with hierarchical structure as a high-efficiency electromagnetic wave absorber, J. Alloys Compd. 846 (2020), 156215, https://doi.org/10.1016/j.jallcom.2020.156215.
[8] X. Di, Y. Wang, Y. Fu, X. Wu, P. Wang, Wheat flour-derived nanoporous carbon@ZnFe2O4 hierarchical composite as an outstanding microwave absorber, Carbon N. Y. 173 (2021) 174–184, https://doi.org/10.1016/j.carbon.2020.11.006.
[9] Ting Jin, Huangxu Li, Kunjie Zhu, Peng-Fei Wang, Pei Liu, Lifang Jiao, Polyanion-type cathode materials for sodium-ion batteries, Chem. Soc. Rev. 49 (8) (2020) 2342–2377, https://doi.org/10.1039/C9CS00846B.
[10] E. Boivin, J.N. Chotard, T. Bamine, D. Carlier, P. Serras, V. Palomares, T. Rojo, A. Iadecola, L. Dupont, L. Bourgeois, F. Fauth, C. Masquelier, L. Croguennec, Vanadyl-type defects in Tavorite-like NaVPO4F: From the average long range structure to local environments, J. Mater. Chem. A. 5 (2017) 25044–25055, https://doi.org/10.1039/c7ta08733k.
[11] A. Chakraborty, S. Kunnikuruvan, S. Kumar, B. Markovsky, D. Aurbach, M. Dixit, D.T. Major, Layered cathode materials for lithium-ion batteries: Review of computational studies on LiNi1- x- yCoxMnyO2 and LiNi1- x- yCoxAlyO2, Chem. Mater. 32 (2020) 915–952, https://doi.org/10.1021/acs.chemmater.9b04066.
[12] Sorour Semsari Parapari, Jean-Marcel Ateba Mba, Elena Tchernychova, Gregor Mali, Iztok Arčon, Gregor Kapun, Mehmet Ali Gülgün, Robert Dominko, Effects of a mixed O/F ligand in the tavorite-type LiVPO4O structure, Chem. Mater. 32 (1) (2020) 262–272.
[13] G. Shore, D. Gusho, H. Hassan, E. Gjuraj, Microwave-sensitive reactors to the rescue: From microwave-assisted chemistry to environmental applications, Am. J. Appl. Sci. 15 (2018) 278–305, https://doi.org/10.3844/ajassp.2018.278.305.
[14] X. Fan, E. Hu, X. Ji, Y. Zhu, F. Han, S. Hwang, J. Liu, S. Bak, Z. Ma, T. Gao, S. C. Liou, J. Bai, X.Q. Yang, Y. Mo, K. Xu, D. Su, C. Wang, High energy-density and reversibility of iron fluoride cathode enabled via an intercalation-extrusion reaction, Nat. Commun. 9 (2018) 1–12, https://doi.org/10.1038/s41467-018-04476-2.
[15] M.E. Arroyo y de Dompablo, U. Amador, J.-M. Tarascon, A computational investigation on fluorinated-polyanionic compounds as positive electrode for lithium batteries, J. Power Sources 174 (2) (2007) 1251–1257, https://doi.org/10.1016/j.jpowsour.2007.06.178.

[16] K.P. Kirubakaran, C. Senthil, M. Priyadarshini, S. Kamalakannan, M. Prakash, V. Vinesh, B. Neppolian, V. Ganesh, C.W. Lee, K. Vediappan, High energy density of multivalent glass-ceramic cathodes for Li-ion rechargeable cells and as an efficient photocatalyst for organic degradation, Energy Storage (2020), https://doi.org/10.1002/est2.133.
[17] Aravind Baby, Baskar Senthilkumar, Prabeer Barpanda, Low-cost rapid template-free synthesis of nanoscale zinc spinels for energy storage and electrocatalytic applications, ACS Appl. Energy Mater. 2 (5) (2019) 3211–3219.
[18] T.M. and B.F. Fabian Diaz, Yufengnan Wang, Degradation Mechanism of Nickel-Cobalt-Aluminum (NCA) Cathode Material from Spent Lithium-Ion Batteries in Microwave-Assisted Pyrolysis, Metals (Basel). 8 (2018) 565. 10.3390/met8080565.
[19] G. Kresse, J. Furthmüller, Efficiency of ab-initio total energy calculations for metals and semiconductors using a plane-wave basis set, Comput. Mater. Sci. 6 (1) (1996) 15–50, https://doi.org/10.1016/0927-0256(96)00008-0.
[20] G. Kresse, J. Furthmüller, Efficient iterative schemes for ab initio total-energy calculations using a plane-wave basis set, Phys. Rev. B - Condens. Matter Mater. Phys. 54 (16) (1996) 11169–11186, https://doi.org/10.1103/PhysRevB.54.11169.
[21] P.E. Blöchl, Projector augmented-wave method, Phys. Rev. B. 50 (24) (1994) 17953–17979, https://doi.org/10.1103/PhysRevB.50.17953.
[22] G. Kresse, D. Joubert, From ultrasoft pseudopotentials to the projector augmented-wave method, Phys. Rev. B - Condens. Matter Mater. Phys. 59 (3) (1999) 1758–1775, https://doi.org/10.1103/PhysRevB.59.1758.
[23] John P. Perdew, Kieron Burke, Matthias Ernzerhof, Generalized Gradient Approximation Made Simple John, Phys. Rev. Lett. 77 (18) (1996) 3865–3868, https://doi.org/10.1103/PhysRevLett.77.3865.
[24] Jochen Heyd, Gustavo E. Scuseria, Matthias Ernzerhof, Hybrid functionals based on a screened Coulomb potential, J. Chem. Phys. 118 (18) (2003) 8207–8215, https://doi.org/10.1063/1.1564060.
[25] J. Heyd, G.E. Scuseria, M. Ernzerhof, Erratum: Hybrid functionals based on a screened Coulomb potential, J. Chem. Phys. 124 (2006), https://doi.org/10.1063/1.2204597.
[26] James D. Pack, Hendrik J. Monkhorst, "special points for Brillouin-zone integrations"-a reply, Phys. Rev. B. 16 (4) (1977) 1748–1749.
[27] S.H. Chen, Z.R. Xiao, Y.P. Liu, P.H. Lee, Y.K. Wang, Journal of Magnetism and Magnetic Materials First-principle calculation on nearly half-metallic antiferromagnetic behavior of double perovskites La 2 VReO 6, J. Magn. Magn. Mater. 323 (1) (2011) 175–178, https://doi.org/10.1016/j.jmmm.2010.08.059.
[28] M.M. Islam, M. Wilkening, P. Heitjans, T. Bredow, Insights into Li + migration pathways in α - Li 3 VF 6: A first-principles investigation, J. Phys. Chem. Lett. 3 (2012) 3120–3124, https://doi.org/10.1021/jz3014198.
[29] Fengzhu Ren, Jihua Zhang, Yuanxu Wang, Wenzhi Yao, A graphene-coupled Bi2WO6 nanocomposite with enhanced photocatalytic performance: A first-principles study, Phys. Chem. Chem. Phys. 18 (20) (2016) 14113–14121, https://doi.org/10.1039/C6CP00458J.
[30] Q. Wang, A. Sarkar, D. Wang, L. Velasco, R. Azmi, S.S. Bhattacharya, T. Bergfeldt, A. Düvel, P. Heitjans, T. Brezesinski, H. Hahn, B. Breitung, Multi-anionic and -cationic compounds: New high entropy materials for advanced Li-ion batteries, Energy Environ. Sci. 12 (2019) 2433–2442, https://doi.org/10.1039/c9ee00368a.
[31] S. Oswald, F. Thoss, M. Zier, M. Hoffmann, T. Jaumann, M. Herklotz, K. Nikolowski, F. Scheiba, M. Kohl, L. Giebeler, D. Mikhailova, H. Ehrenberg, Binding energy referencing for XPS in Alkali metal-based battery materials research (II): Application to complex composite electrodes, Batteries. 4 (2018) 36, https://doi.org/10.3390/batteries4030036.
[32] K.N. Wood, G. Teeter, XPS on Li-battery-related compounds: Analysis of inorganic SEI phases and a methodology for charge correction, ACS Appl. Energy Mater. 1 (2018) 4493–4504, https://doi.org/10.1021/acsaem.8b00406.
[33] R. Guo, X. Liu, B. Wen, F. Liu, J. Meng, P. Wu, J. Wu, Q. Li, L. Mai, Engineering mesoporous structure in amorphous carbon boosts potassium storage with high initial coulombic efficiency, Nano-Micro Lett. 12 (2020), https://doi.org/10.1007/s40820-020-00481-7.
[34] F. Jiang, Y. Di, E. Liu, S. Chen, F. Chen, X. Zhu, X. Wang, Z. Lu, D. Huang, First-principles investigation of the structural stability and electronic properties of LiV 1–x M x PO 4 F (M = Mn, Fe Co, and Ni), J. Solid State Electrochem. 24 (2020) 1075–1084, https://doi.org/10.1007/s10008-020-04582-6.
[35] S. Liu, L. Kang, J.M. Kim, Y.T. Chun, J. Zhang, S.C. Jun, Recent advances in vanadium-based aqueous rechargeable zinc-ion batteries, Adv. Energy Mater. (2020) 1–71, https://doi.org/10.1002/aenm.202000477.
[36] Edouard Boivin, Antonella Iadecola, François Fauth, Jean-Noël Chotard, Christian Masquelier, Laurence Croguennec, The redox paradox of Vanadium in Tavorite LiVPO4F1-yOy, Chem. Mater. 31 (18) (2019) 7367–7376.
[37] Da Deng, Transition metal oxyfluorides for next-generation rechargeable batteries, Chem. Nano Mat. 3 (3) (2017) 146–159, https://doi.org/10.1002/cnma.201600342.
[38] C. Ding, T. Liu, X. Yan, L. Huang, S. Ryu, J. Lan, Y. Yu, W.H. Zhong, X. Yang, An ultra-microporous carbon material boosting integrated capacitance for cellulose-based supercapacitors, Nano-Micro Lett. 12 (2020), https://doi.org/10.1007/s40820-020-0393-7.
[39] L. Wang, J. Han, D. Kong, Y. Tao, Q.H. Yang, Enhanced roles of carbon architectures in high-performance lithium-ion batteries, Nano-Micro Lett. 11 (2019) 1–23, https://doi.org/10.1007/s40820-018-0233-1.
[40] Qiao Huang, Kostiantyn Turcheniuk, Xiaolei Ren, Alexandre Magasinski, Ah-Young Song, Yiran Xiao, Doyoub Kim, Gleb Yushin, Cycle stability of conversion-type iron fluoride lithium battery cathode at elevated temperatures in polymer electrolyte composites, Nat. Mater. 18 (12) (2019) 1343–1349, https://doi.org/10.1038/s41563-019-0472-7.
[41] Fushan Geng, Bei Hu, Chao Li, Chong Zhao, Olivier Lafon, Julien Trébosc, Jean-Paul Amoureux, Ming Shen, Bingwen Hu, Anionic redox reactions and structural degradation in a cation-disordered rock-salt Li1.2Ti0.4Mn0.4O2cathode material revealed by solid-state NMR and EPR, J. Mater. Chem. A. 8 (32) (2020) 16515–16526, https://doi.org/10.1039/D0TA03358H.
[42] Duho Kim, Jangmin Lee, Anionic redox reactions in manganese-based binary layered oxides for advanced sodium-ion batteries, Chem. Mater. 32 (13) (2020) 5541–5549.
[43] Bing-Ang Mei, Obaidallah Munteshari, Jonathan Lau, Bruce Dunn, Laurent Pilon, Physical interpretations of nyquist plots for EDLC electrodes and devices, J. Phys. Chem. C. 122 (1) (2018) 194–206.
[44] Minkyung Kim, Mihee Jeong, Won-Sub Yoon, Byoungwoo Kang, Ultrafast kinetics in a phase separating electrode material by forming an intermediate phase without reducing the particle size, Energy Environ. Sci. 13 (11) (2020) 4258–4268.
[45] A. Lee, M. Vörös, W.M. Dose, J. Niklas, O. Poluektov, R.D. Schaller, H. Iddir, V. A. Maroni, E. Lee, B. Ingram, L.A. Curtiss, C.S. Johnson, Photo-accelerated fast charging of lithium-ion batteries, Nat. Commun. 10 (2019) 1–7, https://doi.org/10.1038/s41467-019-12863-6.
[46] K. Zou, P. Cai, B. Wang, C. Liu, J. Li, T. Qiu, G. Zou, H. Hou, X. Ji, Insights into enhanced capacitive behavior of carbon cathode for lithium ion capacitors: The coupling of pore size and graphitization engineering, Nano-Micro Lett. 12 (2020), https://doi.org/10.1007/s40820-020-00458-6.
[47] Z. Wang, S. Zeng, J. Guo, T. Qin, Remaining capacity estimation of lithium-ion batteries based on the constant voltage charging profile, PLoS One. 13 (2018) 1–22, https://doi.org/10.1371/journal.pone.0200169.
[48] Huiwen Ji, Jinpeng Wu, Zijian Cai, Jue Liu, Deok-Hwang Kwon, Hyunchul Kim, Alexander Urban, Joseph K. Papp, Emily Foley, Yaosen Tian, Mahalingam Balasubramanian, Haegyeom Kim, Raphaële J. Clément, Bryan D. McCloskey, Wanli Yang, Gerbrand Ceder, Ultrahigh power and energy density in partially ordered lithium-ion cathode materials, Nat. Energy. 5 (3) (2020) 213–221, https://doi.org/10.1038/s41560-020-0573-1.
[49] Chengyi Lu, David W. Rooney, Xiong Jiang, Wang Sun, Zhenhua Wang, Jiajun Wang, Kening Sun, Achieving high specific capacity of lithium-ion battery cathodes by modification with "n-O" radicals and oxygen-containing functional groups, J. Mater. Chem. A. 5 (47) (2017) 24636–24644, https://doi.org/10.1039/C7TA08688A.
[50] B. Ji, F. Zhang, M. Sheng, X. Tong, Y. Tang, A novel and generalized lithium-ion-battery configuration utilizing al foil as both anode and current collector for enhanced energy density, Adv. Mater. 29 (2017) 1–7, https://doi.org/10.1002/adma.201604219.
[51] Y. Abe, N. Hori, S. Kumagai, Electrochemical impedance spectroscopy on the performance degradation of LiFePO4/graphite lithium-ion battery due to charge-discharge cycling under different c-rates, Energies. 12 (2019) 1–14, https://doi.org/10.3390/en12234507.
[52] S. Wirths, K. Weis, A. Winden, K. Sladek, C. Volk, S. Alagha, T.E. Weirich, M. Von Der Ahe, H. Hardtdegen, H. Lüth, N. Demarina, D. Grützmacher, T. Schäpers, Effect of Si-doping on InAs nanowire transport and morphology, J. Appl. Phys. 110 (2011), https://doi.org/10.1063/1.3631026.
[53] Subrahmanyam Goriparti, Ermanno Miele, Mirko Prato, Alice Scarpellini, Sergio Marras, Simone Monaco, Andrea Toma, Gabriele C. Messina, Alessandro Alabastri, Francesco De Angelis, Liberato Manna, Claudio Capiglia, Remo Proietti Zaccaria, Direct synthesis of carbon-doped TiO2-bronze nanowires as anode materials for high performance lithium-ion batteries, ACS Appl. Mater. Interfaces. 7 (45) (2015) 25139–25146, https://doi.org/10.1021/acsami.5b06426.
[54] Fangwei Peng, Deying Mu, Ruhong Li, Yuanlong Liu, Yuanpeng Ji, Changsong Dai, Fei Ding, Impurity removal with highly selective and efficient methods and the recycling of transition metals from spent lithium-ion batteries, RSC Adv. 9 (38) (2019) 21922–21930, https://doi.org/10.1039/C9RA02331C.
[55] WenWu Zhong, Jingdong Huang, Shuquan Liang, Jun Liu, Yejing Li, Gemei Cai, Yong Jiang, Jun Liu, New prelithiated V2O5 superstructure for lithium-ion batteries with long cycle life and high power, ACS Energy Lett. 5 (1) (2020) 31–38.